Downloaded from orbit.dtu.dk on: May 06, 2023

DTU Library

Large scale three-dimensional topology optimisation of heat sinks cooled by natural convection

Alexandersen, Joe; Sigmund, Ole; Aage, Niels

Published in:
International Journal of Heat and Mass Transfer

Link to article, DOI:
10.1016/j.ijheatmasstransfer.2016.05.013

Publication date:
2016

Document Version
Peer reviewed version

Link back to DTU Orbit

Citation (APA):
Alexandersen, J., Sigmund, O., & Aage, N. (2016). Large scale three-dimensional topology optimisation of heat sinks cooled by natural convection. *International Journal of Heat and Mass Transfer*, *100*, 876-891. https://doi.org/10.1016/j.ijheatmasstransfer.2016.05.013

General rights
Copyright and moral rights for the publications made accessible in the public portal are retained by the authors and/or other copyright owners and it is a condition of accessing publications that users recognise and abide by the legal requirements associated with these rights.

- Users may download and print one copy of any publication from the public portal for the purpose of private study or research.
- You may not further distribute the material or use it for any profit-making activity or commercial gain
- You may freely distribute the URL identifying the publication in the public portal

If you believe that this document breaches copyright please contact us providing details, and we will remove access to the work immediately and investigate your claim.

Large scale three-dimensional topology optimisation of heat sinks cooled by natural convection

Joe Alexandersen[a,*], Ole Sigmund[a], Niels Aage[a]

[a]*Department of Mechanical Engineering, Solid Mechanics*
Technical University of Denmark
Nils Koppels Allé, Building 404
DK-2800, Denmark

Abstract

This work presents the application of density-based topology optimisation to the design of three-dimensional heat sinks cooled by natural convection. The governing equations are the steady-state incompressible Navier-Stokes equations coupled to the thermal convection-diffusion equation through the Bousinessq approximation. The fully coupled non-linear multiphysics system is solved using stabilised trilinear equal-order finite elements in a parallel framework allowing for the optimisation of large scale problems with order of 20-330 million state degrees of freedom. The flow is assumed to be laminar and several optimised designs are presented for Grashof numbers between 10^3 and 10^6. Interestingly, it is observed that the number of branches in the optimised design increases with increasing Grashof numbers, which is opposite to two-dimensional topology optimised designs. Furthermore, the obtained topologies verify prior conclusions regarding fin length/thickness ratios and Biot numbers, but also indicate that carefully tailored and complex geometries may improve cooling behaviour considerably compared to simple heat fin geometries.

Keywords: topology optimisation, heat sink design, natural convection, large scale, multiphysics optimisation

1. Introduction

Natural convection is the phenomena where density-gradients due to temperature differences cause a fluid to move. Natural convection is therefore a natural way to passively cool a hot object, such as electronic components, light-emitting diode (LED) lamps or materials in food processing.

Structural optimisation is the discipline of modifying the design of a structure in order to improve its performance with respect to some desirable behaviour. Structural optimisation techniques, such as size and configuration optimisation, are very efficient if a close-to-optimal design is already known, or the topology of the structure is dictated by e.g. certain manufacturing methods. These methods are frequently applied to the design of heat sinks in electronics cooling. The following literature review is by no means complete, giving only representative examples: Morrison [1] optimises plate fin heat sinks in natural convection using a downhill simplex method and empirical correlations. The design variables are the fin thickness, fin spacing and backplate thickness; Ladezma and Bejan [2] investigate the geometric arrangement of staggered vertical plates in natural convection using numerical simulations. The design variables are various dimensions of the staggered arrangement; Iyengar and Bar-Cohen [3] investigate vertical pin-fin, plate-fin and triangular-fin heat sinks in natural convection using analytical and empirical correlations. The design variables are the fin thickness and spacing; Bahadur and Bar-Cohen [4] optimise staggered pin fin heat sinks for natural convection cooled microprocessor applications using analytical equations. The design variables are pin height, diameter and spacing; Jang et al. [5] optimise radial pin-fin heat sinks for LED applications using numerical simulation and a genetic algorithm. The design variables are the number of and length of fins. Furthermore, there exists a vast literature treating optimal structures for surface-to-point and volume-to-point heat generation, e.g. [6], but these do not consider convective heat transfer and are thus not directly relevant to the problems at hand.

While parameter studies and simple optimisation techniques, like the above mentioned, can provide insight and improvements to existing designs, they are all limited in their design freedom as an *a priori* determined initial design must be given. Topology optimisation allows for a vastly expanded design space, allowing for the formation of unintuitive and unanticipated designs that fully exploit the governing physics. Topology optimisation is a material distribution method [7, 8, 9] used to optimise the layout of a structure. In order to take convective heat transfer, to an ambient fluid, into account in the design process of density-based methods, a common extension is to introduce some form of interpolation of the convection boundaries, see e.g. [10, 11, 12, 13]. More recently, these simplified models have been used by Dede et al. [14] to design and manufacture heat sinks subject to jet impingement cooling, as well as by Zhou et al. [15] in an industrial framework to optimise electric motor covers and heat sinks.

Generally, the application of a predetermined and design-

*Corresponding author
Email address: joealex@mek.dtu.dk (Joe Alexandersen)

independent convection coefficient is at best inaccurate and may have a strong influence on resulting designs and their performance. In practise, topology optimisation based on simplified models may lead to unanticipated designs and closed cavities, thereby violating the assumptions of the simplified model [16]. During the optimisation process, the design changes significantly and the interaction with the ambient fluid changes as well. Therefore, to ensure physically correct capturing of the aspects of convective heat transfer, the full conjugate heat transfer problem must be solved. Obviously, the employment of a full-blown fluid model increases computational time and complexity considerably. Hence, using the simplified convection approach, that provides for very fast solution times, may likely provide a good first estimate for an optimised topology or may be used for post-processing once topology and associated local convection coefficients have been found. Furthermore, it may be beneficial to use the simplified convection approach, when the flow is too complex to model in current optimisation settings (hundreds or thousands of function evaluations). Please see [13, 16, 17, 18, 15] for further discussions on the strengths and weaknesses of using the simplified convection approach.

Topology optimisation for fluid systems began with the treatment of Stokes flow in the seminal article by Borrvall and Petersson [19] and has since been applied to Navier-Stokes [20], as well as passive transport problems [21, 22], reactive flows [23], transient flows [24, 25, 26], fluid-structure interaction [27, 28], amongst many others. The extension of topology optimisation to turbulent fluid flow is very much in its infancy [29] and requires further research. Conjugate heat transfer problems were first treated in [30, 31] and is very much an active field of research today [32, 33, 34, 35, 36, 37]. However, almost all work is focused on forced convection, where the fluid flow is induced by a fan, pump or pressure-gradient. The authors have previously presented a density-based topology optimisation approach for two-dimensional natural convection problems [18]. Recently, Coffin and Maute presented a level-set method for steady-state and transient natural convection problems using the eXtended finite element method (X-FEM) [38]. Interested readers are referred to [18] for further references and a deeper introduction to topology optimisation in fluid dynamics and heat transfer.

Throughout this article, the flows are assumed to be steady and laminar. The fluid is assumed to be incompressible, but buoyancy effects are taken into account through the Boussinesq approximation, which introduces variations in the fluid density due to temperature gradients. The inclusion of a Brinkman friction term facilitates the topology optimisation of the fluid flow.

The scope of this article is primarily to present and provide basic verifications of a large scale, three-dimensional framework for topology optimisation of thermal heat sinks. The methodology builds on the two-dimensional framework presented in [18]. Thus, only a brief overview of the underlying finite element and topology optimisation formulation is given and the reader is referred to [18] for further information. The numerical extension to three dimensions is non-trivial and hence the present article includes new discussions on interpolation and continuation strategies, as well as on computational issues arising from solving the large-scale, non-linear equation systems considered. In this first application of topology optimisation to natural convection problems in three dimensions, dimensionless parameters and fictitious properties are used. Nevertheless, interesting insight will be gained on the effect of Grashof number in optimal design. Ongoing and future work is devoted to the treatment of physically realistic problems for LED lamp coolers [39] and other practical devices.

In recent years an increasing body of work has been published on efficient large scale topology optimisation. These works cover the use of high-level scripting languages [40, 41], multiscale/-resolution approaches [42, 43] and parallel programming using the message parsing interface (MPI) and C/Fortran [44, 45, 46, 47]. To facilitate the solution to truly large scale conjugate heat transfer problems, the implementation in this article is done using PETSc [48] and the framework for topology optimisation presented in [47].

The layout of the article is as follows: Section 2 presents the governing equations; Section 3 presents the topology optimisation problem; Section 4 briefly discusses the finite element formulation; Section 5 discusses the numerical implementation details; Section 6 presents scalability results for the parallel framework, optimised designs for two test problems, as well as verification results; Section 7 finishes with a discussion and conclusion.

2. Governing equations

The dimensionless form of the governing equations have been derived based on the Navier-Stokes and convection-diffusion equations under the assumption of constant fluid properties, incompressible, steady flow and neglecting viscous dissipation. Furthermore, the Boussinesq approximation has been introduced to take density-variations due to temperature-differences into account. A domain is decomposed into two subdomains, $\Omega = \Omega_f \cup \Omega_s$, where Ω_f is the fluid domain and Ω_s is the solid domain. In order to facilitate the topology optimisation of conjugate natural convective heat transfer between a solid and a surrounding fluid, the equations are posed in the unified domain, Ω, and the subdomain behaviour is achieved through the control of coefficients. The following dimensionless composite equations are the result.
$\forall \mathbf{x} \in \Omega$:

$$u_j \frac{\partial u_i}{\partial x_j} - Pr \frac{\partial}{\partial x_j}\left(\frac{\partial u_i}{\partial x_j} + \frac{\partial u_j}{\partial x_i}\right) + \frac{\partial p}{\partial x_i} = -\alpha(\mathbf{x}) u_i - GrPr^2\, e_i^g\, T \tag{1}$$

$$\frac{\partial u_j}{\partial x_j} = 0 \tag{2}$$

$$u_j \frac{\partial T}{\partial x_j} - \frac{\partial}{\partial x_j}\left(K(\mathbf{x}) \frac{\partial T}{\partial x_j}\right) = s(\mathbf{x}) \tag{3}$$

where u_i is the velocity field, p is the pressure field, T is the temperature field, x_i denotes the spatial coordinates, e_i^g is the unit vector in the gravitational direction, $\alpha(\mathbf{x})$ is the spatially-varying effective impermeability, $K(\mathbf{x})$ is the spatially-varying

effective thermal conductivity, $s(\mathbf{x})$ is the spatially-varying volumetric heat source term, Pr is the Prandtl number, and Gr is the Grashof number.

The effective thermal conductivity, $K(\mathbf{x})$, is defined as:

$$K(\mathbf{x}) = \begin{cases} 1 & \text{if } \mathbf{x} \in \Omega_f \\ \frac{1}{C_k} & \text{if } \mathbf{x} \in \Omega_s \end{cases} \tag{4}$$

where $C_k = \frac{k_f}{k_s}$ is the ratio between the fluid thermal conductivity, k_f, and the solid thermal conductivity, k_s. Theoretically, the effective impermeability, $\alpha(\mathbf{x})$, is defined as:

$$\alpha(\mathbf{x}) = \begin{cases} 0 & \text{if } \mathbf{x} \in \Omega_f \\ \infty & \text{if } \mathbf{x} \in \Omega_s \end{cases} \tag{5}$$

in order to ensure zero velocities inside the solid domain. However, numerically this requirement must be relaxed as will be described in section 3. The volumetric heat source term is defined as being active within a predefined subdomain of the solid domain, $\omega \subset \Omega_s$:

$$s(\mathbf{x}) = \begin{cases} 0 & \text{if } \mathbf{x} \notin \omega \\ s_0 & \text{if } \mathbf{x} \in \omega \end{cases} \tag{6}$$

where $s_0 = \frac{qL^2}{k_f \Delta T}$ is the dimensionless volumetric heat generation, q is the dimensional volumetric heat generation, ΔT is the reference temperature difference and L is the reference length scale.

The Prandtl number is defined as:

$$Pr = \frac{\nu}{\Gamma} \tag{7}$$

where ν is the kinematic viscosity, or momentum diffusivity, and Γ is the thermal diffusivity. It thus describes the relative spreading of viscous and thermal effects. The Grashof number is defined as:

$$Gr = \frac{g\beta\,\Delta T\,L^3}{\nu^2} \tag{8}$$

where g is the acceleration due to gravity and β is the volumetric coefficient of thermal expansion. It describes the ratio between the buoyancy and viscous forces in the fluid. The Grashof number is therefore used to describe to what extent the flow is dominated by natural convection or diffusion. For low Gr the flow is dominated by viscous diffusion and for high Gr the flow is dominated by natural convection. The problems in this article are assumed to have large enough buoyancy present to exhibit natural convective effects, but small enough Gr numbers to exhibit laminar fluid motion.

3. Optimisation formulation

3.1. Interpolation functions

In order to perform topology optimisation, a continuous design field, $\gamma(\mathbf{x})$, varying between 0 and 1 is introduced. Pure fluid is represented by $\gamma(\mathbf{x}) = 1$ and solid by $\gamma(\mathbf{x}) = 0$. For intermediate values between 0 and 1, the effective conductivity is interpolated as follows:

$$K(\gamma) = \frac{\gamma(C_k(1+q_f)-1)+1}{C_k(1+q_f\gamma)} \tag{9}$$

and likewise the effective impermeability is interpolated using:

$$\alpha(\gamma) = \overline{\alpha}\frac{1-\gamma}{1+q_\alpha\gamma} \tag{10}$$

The interpolation functions ensure that the end points defined in (4) and (5), respectively, are satisfied. The effective impermeability is bounded to $\overline{\alpha}$ in the solid regions and this upper bound should be chosen large enough to provide vanishing velocities, but small enough to ensure numerical stability. The convexity factors, q_f and q_α, are used to control the material properties for intermediate design values in order to promote well-defined designs without intermediate design field values.

3.2. Optimisation problem

The topology optimisation problem is defined as:

$$\begin{aligned} \underset{\gamma\in\mathcal{D}}{\text{minimise:}} & f(\gamma, T) = \int_\omega s(\mathbf{x})\,T\,dV \\ \text{subject to: } & g(\gamma) = \int_{\Omega_d} 1-\gamma\,dV \le v_f \int_{\Omega_d} dV \\ & \mathscr{R}(\gamma, \mathbf{u}, p, T) = 0 \\ & 0 \le \gamma(\mathbf{x}) \le 1 \quad \forall \mathbf{x} \in \Omega_d \end{aligned} \tag{11}$$

where γ is the design variable field, $\mathcal{D}$ is the design space, f is the thermal compliance objective functional, g is the volume constraint functional, $\mathscr{R}(\gamma, \mathbf{u}, p, T)$ is the residual arising from the stabilised weak form of the governing equations, and $\Omega_d \subseteq \Omega$ is the design domain.

The design field is regularised using a PDE-based (partial differential equation) density filter [49, 47] and the optimisation problem is solved using the method of moving asymptotes (MMA) [50, 47].

3.3. Continuation scheme

A continuation scheme is performed on various parameters in order to stabilise the optimisation process and to improve the optimisation results. It is the experience of the authors that the provided continuation scheme yields better results than starting with the end values, although this cannot generally be proven [51, 52].

The chosen continuation strategy consists of five steps:

$$q_f \in \{0.881, 8.81, 88.1, 881, 881\} \tag{12a}$$

$$q_\alpha \in \{8, 8, 8, 98, 998\} \tag{12b}$$

$$\overline{\alpha} \in \left\{10^5, 10^5, 10^5, 10^6, 10^7\right\} \tag{12c}$$

The sequence is chosen in order to alleviate premature convergence to poor local minima. The value of q_f is slowly increased to penalise intermediate design field values with respect to conductivity. The maximum effective permeability, $\overline{\alpha}$, is set relatively low during the first three steps, as this ensures better

scaled sensitivities and more stable behaviour. Over the last two steps, $\overline{\alpha}$ is increased by two orders of magnitude in order to further decrease the velocity magnitudes in the solid regions. The particular values of q_f and q_α are chosen by empirical inspection, such as to ensure the approximate collocation of the fluid and thermal boundaries. The suggested continuation strategy is based on extensive numerical studies and experiments reflecting that: a) a high initial $\bar{\alpha}$ causes designs to glue to outer walls of the design domain; b) a high initial q_f causes too rapid convergence to 0-1 solutions; c) starting with final values for all parameters gives bad scaling of initial sensitivities and hence convergence towards inferior local optima. Here, it is important to note that the optimisation problem is by no means convex and any optimised design will at best be a local minimum. The obtained design will always depend on the initial design as well as the continuation strategy. However, in the authors experience, the chosen continuation strategy gives a good balance between convergence speed, final design performance and physicality of the modelling. The effects of the steps of the current continuation strategy on the design distribution will be discussed in section 6.5. Also, it is noted that results obtained using the suggested continuation strategy: a) indicate that consistent and well-performing designs are obtained as verified by cross-checks; b) indicate that boundary effects are captured sufficiently accurately as verified by COMSOL runs based on body-fitted meshes and accurate boundary conditions, see section 6.4.

4. Finite element formulation

The governing equations are discretised using stabilised trilinear hexahedral finite elements. The design field is discretised using elementwise constant variables, in turn rendering the effective thermal conductivity and the effective impermeability to be elementwise constant. The monolithic finite element discretisation of the problem ensures continuity of the temperature field, as well as the fluxes across fluid-solid interfaces. The particularities of the implemented finite element formulation are as detailed in [18]. However, simpler stabilisation parameters have been used in order to allow for consistent sensitivities to be employed, see Appendix A. The Jacobian matrix is now fully consistent, in that variations of the stabilisation parameters with respect to design and state fields are included, in contrast to the original work [18].

5. Numerical implementation

The discretised FEM equation is implemented in PETSc [48] based on the topology optimisation framework presented in [47]. The PETSc framework is used due to its parallel scalability, the availability of both linear and non-linear solvers, preconditioners and structured mesh handling possibilities. All components described in the following are readily available within the PETSc framework.

5.1. Solving the non-linear system

The non-linear system of equations is solved using a damped Newton method. The damping coefficient is updated using a polynomial L^2-norm fit, where the coefficient is chosen as the minimiser of the polynomial fit. The polynomial fit is built using the L^2-norm of the residual vector at the current solution point, at 50% of the Newton step and at 100% of the Newton step. This residual-based update scheme combined with a good initial vector (the solution from the previous design iteration) has been observed to be very robust throughout the optimisation process for the moderately non-linear problems treated. To further increase the robustness of the non-linear solver, if the Newton solver fails from the supplied initial vector, a ramping scheme for the heat generation magnitude is applied in order to recover. Throughout, the convergence criteria for the Newton solver is set to a reduction in the L^2-norm of the residual of 10^{-4} relative to the initial residual.

5.2. Solving the linear systems

Due to the large scale and three-dimensional nature of the treated problems, the arising linearised systems of equations and their solutions are by far the most time consuming part of the Newton scheme. Therefore, to make large scale problems tractable the (unsymmetric) linear systems are solved using a fully parallelised iterative Krylov subspace solver.

Constructing an iterative solver that is independent of problem settings and at the same time possesses both parallel and numerical scalability, is intricate and beyond the scope of this work, where focus is on the optimisation. However, in order to facilitate the solution of large scale optimisation problems, an efficient solver is required. To this end the authors use the readily available core components in PETSc to construct a solver with focus on simplicity, as well as reduced wall clock time. This is quite easy to obtain for solvers and preconditioners that rely heavily on matrix-vector multiplications. To this purpose the flexible GMRES (F-GMRES) method is used as the linear solver combined with a geometry-based Galerkin-projection multigrid (GMG) preconditioner. Such a solver depends highly on the quality of the smoother to guarantee fast convergence [53]. The authors have found that a simple Jacobi-preconditioned GMRES provides a reasonable choice of smoother[1]. The convergence criterion for the Krylov solver is set to 10^{-5} relative to the initial residual.

6. Results

6.1. Problem setup

The considered optimisation problem is an (academic) example of a heat sink in a closed cubic cavity. Figure 1 shows the problem setup with dimensions and boundary conditions. The heat source (black in figure), exemplifying an electronics chip, is placed in the mid-bottom of the cavity and modelled using a

[1] Due to the choice of a Krylov smoother, the multigrid preconditioner will vary slightly with input and thus require a flexible outer Krylov method.

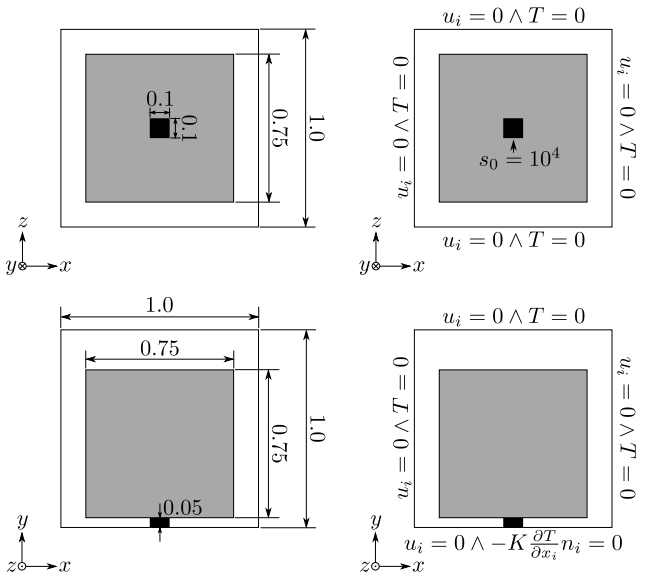

(a) Dimensions (b) Boundary conditions

Figure 1: Illustration of the problem setup for the heat sink in a close cubic cavity. The heat source is black and the design domain is gray.

small block of solid material with volumetric heat generation, $s_0 = 10^4$. The design domain (gray in figure) is placed on top of the heat source in order to allow the cooling fluid to pass underneath it, as well as to allow room for wires etc. The vertical and top outer walls of the cavity are assumed to be kept at a constant cold temperature, $T = 0$, while the bottom is insulated. The height of the cavity has been used as the reference length scale, L. Thus, the cavity dimensions are $1 \times 1 \times 1$, the design domain dimensions are $0.75 \times 0.75 \times 0.75$ and the heat source dimensions are $0.1 \times 0.05 \times 0.1$. A discussion on the definition of the temperature difference in the Grashof number can be found in Appendix B. Initial investigations showed that due to the symmetry of the domain and boundary conditions, the design and state solutions remained quarter symmetric throughout the optimisation. Thus, the computational domain is limited to a quarter of the domain with symmetry boundary conditions. The volume fraction is set to 5%, i.e. $v_f = 0.05$, for all examples.

6.2. Parallel performance

To demonstrate the parallel performance of the state solver, the optimisation problem is solved on a fixed mesh for different numbers of processes. All computations in this article were performed on a cluster, where each node is equipped with two Intel Xeon e5-2680v2 10-core 2.8GHz processors. The results shown in tables 1 and 2 are averaged over 250 design cycles and show the performance for $Gr = 10^3$ and $Gr = 10^6$, respectively. The data shows that the proposed solver scales almost linearly in terms of speed up, and more importantly that the performance is only slightly affected by the Grashof number.

In order to quantify the degree of numerical scalability, a second study is performed in which the mesh resolution is varied. The study is conducted for both low and high Grashof numbers

Processes	time [s]	scaling
160	53.2	1.00
320	28.9	0.54
640	14.1	0.26

Table 1: Average time taken per state solve over 250 design iterations for $Gr = 10^3$ at a mesh resolution of $80 \times 160 \times 80$.

Processes	time [s]	scaling
160	62.6	1.00
320	31.9	0.51
640	16.5	0.26

Table 2: Average time taken per state solve over 250 design iterations for $Gr = 10^6$ at a mesh resolution of $80 \times 160 \times 80$.

and the average F-GMRES iterations are collected in table 3. The total number of design iterations averaged over was 250, 500 and 1000, respectively, for the three mesh resolutions. The data clearly shows that the computational complexity increases with problem size, and thus that the solver is not numerically scalable. However, since the growth in numerical effort, i.e. the number of F-GMRES iterations, is moderate, it is concluded that the proposed solver is indeed applicable for solving large scale natural convection problems.

6.3. Varying Grashof number

The problem is investigated for varying Gr under constant volumetric heat generation, $s_0 = 10^4$, Prandtl number, $Pr = 1$, and thermal conductivity ratio, $C_k = 10^{-2}$. The purpose of the present study is not to provide a detailed physical example. It is rather to provide phenomenological insight into the effect of changing the governing parameter of the fluid-thermal coupling, namely the Grashof number. However, physical interpretations of tuning the Gr-number, while keeping the dimensionless volumetric heat generation and the Pr-number constant, could be e.g. equivalent to tuning the gravitational strength (going from microgravity towards full gravity) or the dimensional volumetric heat generation. It is important to note that when interpreting the results, the dimensional temperature scale will differ for the two interpretations. While tuning the gravitational strength, the temperature scale remains the same; by varying the magnitude of the volumetric heat generation, the temperature scale varies accordingly[2].

[2]The dimensionless volumetric heat generation is given by $s_0 = \frac{qL^2}{k_f \Delta T}$. Requiring that s_0 remains constant, means that the dimensional volumetric heat generation, q, and the reference temperature difference, ΔT, must vary in unison, i.e. $\frac{q}{\Delta T} = \text{const.}$. An increase in the Gr-number is thus achieved through the increase of ΔT.

Mesh size	$Gr = 10^3$	$Gr = 10^6$
$80 \times 160 \times 80$	7.5	5.6
$160 \times 320 \times 160$	10.1	7.7
$320 \times 640 \times 320$	18.4	15.6

Table 3: Average iterations for the linear solver per state solve over entire design process for $Gr = 10^3$ and $Gr = 10^6$ at varying mesh resolutions.

Gr	Primary	Secondary	Surface area
10^3	12	0	0.887
10^4	8	16	0.853
10^5	8	28	0.834
10^6	8	48	0.846

Table 4: The number of primary and secondary branches, as well as the surface area for the optimised designs of figure 2.

The computational mesh is $160 \times 320 \times 160$ elements yielding a total of $8,192,000$ elements and $41,603,205$ degrees of freedom for the quarter domain. The design domain consists of $3,456,000$ elements and the filter radius is set to 2.5 times the element size.

Figure 2 shows the optimised designs for varying Gr-number with superimposed slices of the corresponding temperature fields. Due to the use of density filtering, the interface between solid and fluid regions for the optimised designs are not exactly described but consists of a layer of intermediate design field values. The optimised design distributions are shown thresholded at $\gamma = 0.05$, which is the approximate location of the computational interface as will be verified in section 6.4. The general characteristics of all the designs are similar, i.e. all designs are "thermal trees" with conductive branches moving the heat away from the heat source. However, it can clearly be seen that the design changes considerably with increasing convection-dominance (increasing Gr). For increasing Gr-number the conductive branches contract, resulting in a smaller spatial extent of the overall heat sink. This intuitively makes sense as the problem goes from one of conduction/diffusion at $Gr = 10^3$ to convection at $Gr = 10^6$. When diffusion dominates, the goal for the branches essentially becomes to conduct the heat directly towards the cold walls. As convection begins to matter, the fluid movement aids the transfer of heat away from the heat sink and the branches do not need to be as long. Instead, the design forms higher vertical interfaces in order to increase surface area parallel to the flow direction and thus increase fluid velocity and enhance overall heat transfer. At the same time the complexity of the designs increases as the importance of convection increases. This can be seen by studying the number of primary and secondary branches. Primary branches are defined as those connected to the heat source directly and secondary branches are those connected to primary branches. Table 4 shows the number of primary and secondary branches of the optimised designs shown in figure 2. The number of primary branches is largest for the diffusion-dominated case, but more or less constant thereafter. However, it can be seen that the number of secondary branches significantly increases as the Gr-number is increased. Table 4 also shows that the total surface area[3] is decreasing for the three lower Gr-numbers and then increases slightly.

It is interesting to note, that the trend of increasing complexity with increasing Gr-number is the reverse of what was observed for two-dimensional problems [18]. There, the complexity of the design decreased as the Gr-number increased. This difference is due to the fact that going into three dimensions allows the fluid to move around and through the design making it more a question of "topology", in contrast to the two-dimensional case, where it is a question of surface shape. Physically, in two dimensions additional branches disturb the flow and thus the heat transfer; in three dimensions, vertical branches improve the heat transfer through an increased vertical surface area. Figure 3 shows the optimised designs for $Gr = 10^3$ and $Gr = 10^6$ from below. The radial extent of the designs are emphasised from these views. It is also seen that the branches for $Gr = 10^6$ are positioned to ensure that the structure is open from below, with the branches forming vertical walls as discussed above.

[3]The surface area is computed using an isosurface at the selected threshold design field value.

	Optimisation Gr			
Analysis Gr	10^3	10^4	10^5	10^6
10^3	8.26	8.27	8.96	9.45
10^4	7.73	7.52	7.98	8.45
10^5	5.95	5.80	5.62	5.76
10^6	4.54	4.49	4.25	4.10

Table 5: Cross-check objective function values for the designs shown in figure 2. The compliance is shown for the full domain, which is 4 times the values for the quarter domain.

Gr	Time	Non-linear: avg. (max)	Linear: contin. steps - avg. (max)
10^3	9:56	1.9 (2)	7.6,8.4,7.8,8.1,18.4 - 10.1 (25)
10^4	10:25	2.0 (3)	8.3,8.6,8.3,8.6,22.7 - 11.3 (29)
10^5	10:28	2.1 (10)	8.4,8.6,8.7,8.2,15.7 - 9.9 (34)
10^6	10:35	2.1 (7)	7.3,7.4,7.5,8.0,8.4 - 7.7 (14)

Table 6: Computational time, average non-linear iterations and linear iterations for the optimised designs of figure 2.

Table 5 shows a cross-check of the objective functions for the optimised designs. It can be seen that all designs optimised for certain flow conditions outperform the other designs for the specified Gr-number.

The optimisations were run for 500 design iterations for each optimised design. Table 6 shows the computational time, average non-linear iterations and linear iterations for the optimised designs of figure 2 using 1280 cores. It can be seen that the computational time only weakly increases as the Gr-number is increased and remains close to 1.2 minutes per design iteration on average. It is interesting to note, that $Gr = 10^6$ seems easier to solve than the others as it exhibits lower average number of linear iterations than all others, as well as a lower maximum number of non-linear iterations than $Gr = 10^5$. Furthermore, it can be seen that due to the Newton method starting from a good initial vector (solution from previous design iteration), only 2 non-linear iterations are needed for most of the design iterations independent of Gr-number.

6.4. Verification of boundary interpolation model

For several reasons it is important to verify the obtained topology optimisation results using an alternative model. Partly,

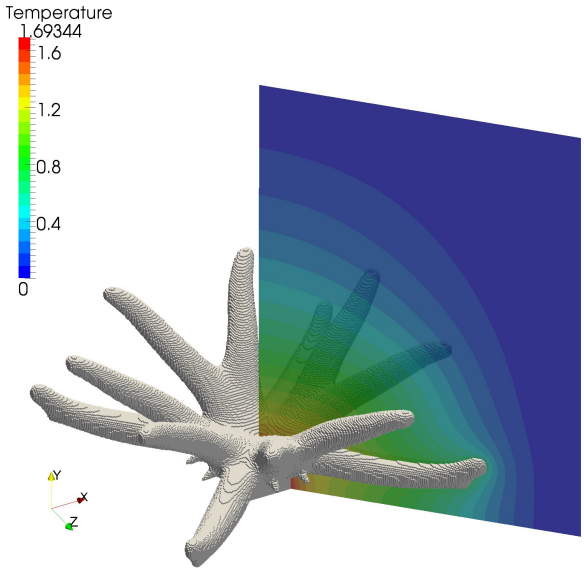

(a) $Gr = 10^3$

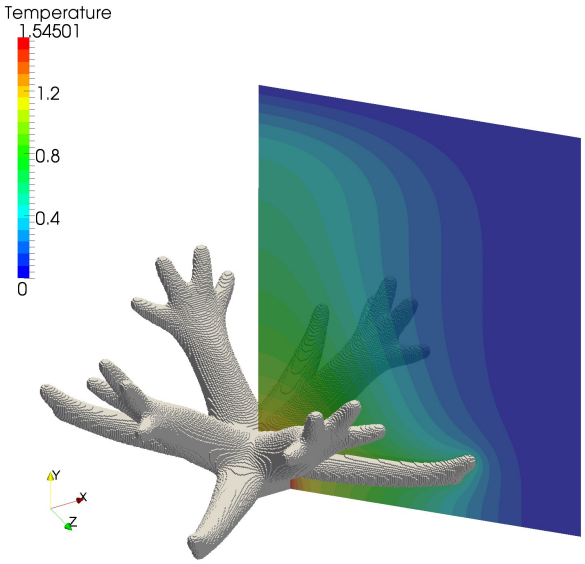

(b) $Gr = 10^4$

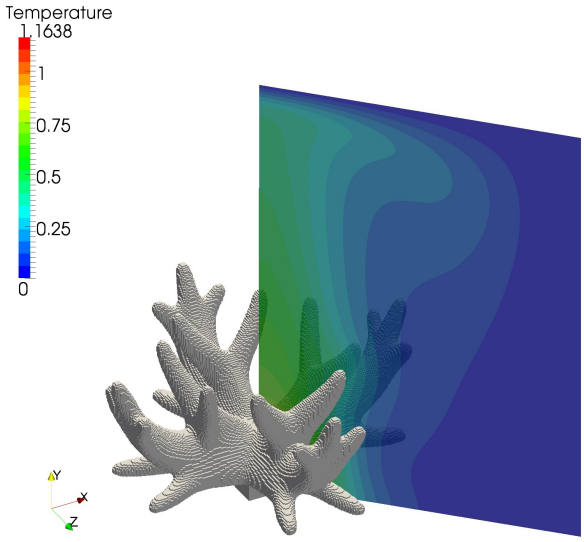

(c) $Gr = 10^5$

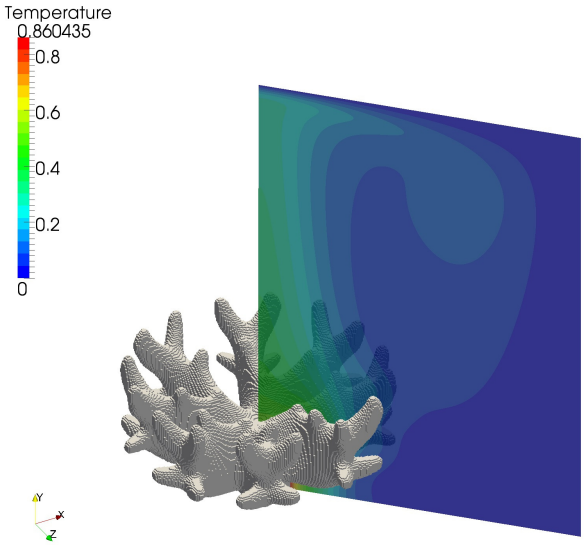

(d) $Gr = 10^6$

Figure 2: Optimised designs for varying Gr-number at a mesh resolution of $160 \times 320 \times 160$.

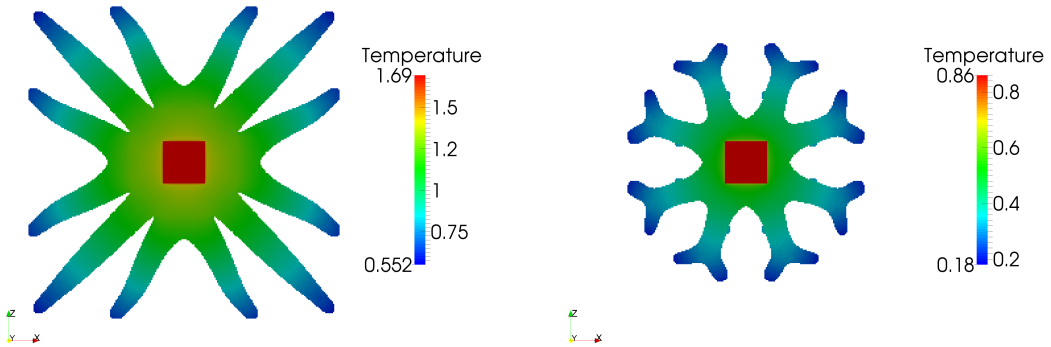

(a) $Gr = 10^3$ (b) $Gr = 10^6$

Figure 3: Temperature distribution in optimised designs for $Gr = 10^3$ and $Gr = 10^6$ at a mesh resolution of $160 \times 320 \times 160$ - view from below.

	Optimisation Gr			
Analysis Gr	10^3	10^4	10^5	10^6
10^3	7.00	7.10	7.96	8.57
10^4	6.54	6.45	6.98	7.51
10^5	4.90	4.86	4.73	4.87
10^6	3.63	3.65	3.46	3.34

Table 7: Cross-check objective function values for the verification of designs shown in figure 2 using COMSOL.

the voxel grid used in the topology optimisation must be verified by a smooth, body-fitted mesh; partly, the Brinkman-type penalisation used to enforce boundary conditions in the topology optimisation must be verified with an exact boundary representation; partly, the threshold value of $\gamma = 0.05$ for converting the continuous density map to a structure with sharp edges must be verified; and partly, the finite element model itself must be verified by a commercial or publicly available software. For these reasons, this section studies the four designs optimised so far using the COMSOL Multiphysics 5.2 finite element-based simulation software.

First, the smoothed designs (isovolumes thresholded at $\gamma = 0.05$) are imported into COMSOL and verifications are run with the same parameters and Grashof numbers as for the topology optimisation model. The full domain is analysed and for all Grashof numbers, the geometry and fluid domain are meshed with a total of approximately $760,000$ tetrahedral elements, where the elements are graded away from surfaces. Figure 4 shows the parametrised geometry for $Gr = 10^6$ after being imported into COMSOL and the corresponding surface mesh used for the verification analysis. A full time-dependent simulation carried out for the $Gr = 10^6$ design shows that a steady state exists. Thus, steady state analyses are performed for the verifications shown.

Table 7 shows a cross-check of the objective functions obtained using COMSOL. It can be seen that all designs optimised for certain flow conditions outperform the other designs for the specified Gr-number and thus, the conclusions of section 6.3 are valid. The objective values for the verification calculations are consistently around 20% lower than the optimisation values from table 5, the reason for which will be discussed below.

In order to verify the accuracy of the topology optimisation approach in further detail, the heat sink geometry for $Gr = 10^6$ is investigated using a finer mesh of $1,566,642$ tetrahedral elements, where refinement has mainly taken place in the fluid domain. For this refined mesh, the objective value is 3.36, which may be compared to the value from the coarser mesh in table 5 of 3.34. This small change indicates that the integral objective value indeed has converged, nevertheless, the finer mesh is used to better capture local boundary effects in the following discussion. Figure 5 shows the temperature and velocity magnitudes as functions of y-coordinate at $(x, z) = (0.57, 0.65)$. This line passes through one of the primary branches of the geometry, as shown in figure 4b. Considering the rather crude treatment of boundary conditions in the topology optimisation model, it can nevertheless be seen that there is very good agreement with the COMSOL verification simulation. The major discrepancy is somewhat surprisingly not found at an interface defined by the optimised structure, but rather at the outer wall ($y = 1$). Here the finer mesh of the topology optimisation model captures the boundary layer better than what is possible with the COMSOL model and its limited resolution capability.

Figure 6 shows a close up of the boundary layers around the design boundaries. Here it can again be seen that the temperature and velocity profiles differ slightly. The most significant difference is for the velocity boundary layer. This difference is mainly due to the Brinkman penalisation used to weakly impose zero velocities inside solid parts and no-slip conditions at the interface. The differences in the temperature level, as well as the objective values in tables 5 and 7, are due to intermediate material at the interface, being upgraded to fully conductive material when thresholded, as clearly seen from figure 6c. The 20% decrease in objective values for the COMSOL models are mainly attributed to this thresholding step. Despite these smaller discrepancies, it is concluded that the topology optimisation model and the associated boundary interpolation model is sufficiently accurate to capture the main effects and ensure that post-processed designs indeed perform as predicted.

If one, despite the above conclusions, would find it pertinent to produce topology optimised structures with sharper edge features and even better quantitative agreement in verification runs, several techniques may be investigated. These techniques in-

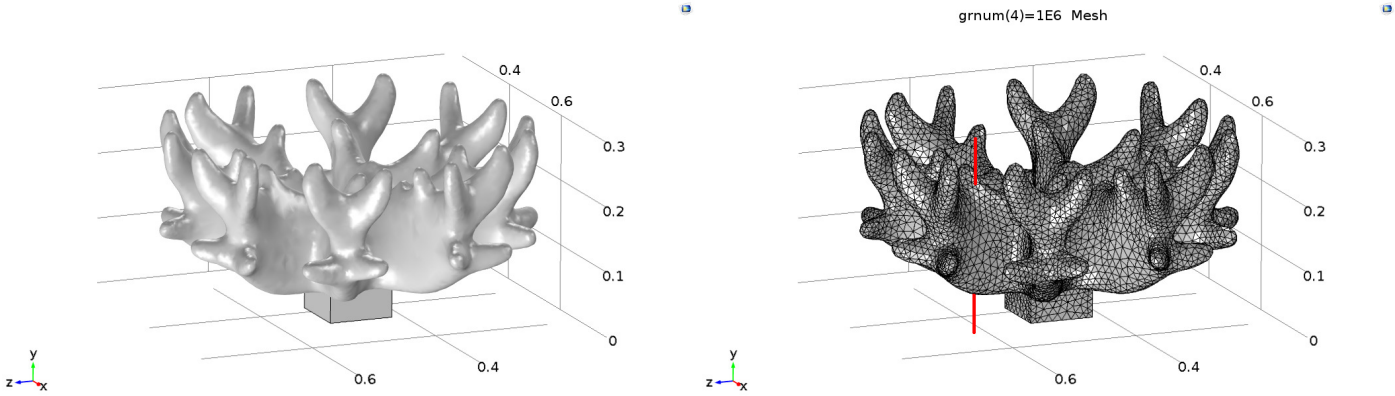

(a) Geometry

(b) Surface mesh

Figure 4: Parametrised geometry and corresponding surface mesh used in the verification analysis for $Gr = 10^6$. The red line shows the line along which the results are compared: a line from $y = 0$ to $y = 1$ at $(x, z) = (0.57, 0.65)$.

	Gr			
	10^3	10^4	10^5	10^6
R_{cond}	8.76×10^{-2}	8.50×10^{-2}	7.21×10^{-2}	6.69×10^{-2}
R_{conv}	1.92×10^{-1}	1.73×10^{-1}	1.17×10^{-1}	6.69×10^{-2}
Bi_{res}	0.46	0.49	0.62	1.00
$\overline{Nu}_L$	6.72	7.69	11.13	19.59

Table 8: Biot numbers and thermal resistances for the verification of designs shown in figure 2.

clude projection methods that ensure length scale (to ensure certain thickness of solid members and fluid channels) [54, 55, 56] or interface capturing schemes, such as X-FEM [38] or discrete simplicial complexes (DSC) [57, 58]. It is important to state, that despite interface capturing schemes providing more accurate modelling, they also carry with them many difficulties with regard to the optimisation [59, 28, 16]. It should be noted that in the authors' experience, a small region of intermediate design variables (ensuring a continuous transition from solid to fluid in all material parameters) is beneficial for numerical stability and accuracy and hence beneficial for the overall convergence of the optimisation algorithm.

Based on the verification runs in COMSOL, further interpretations and insight for the obtained results are given in the following. Table 8 shows the Nusselt and Biot numbers, as well as thermal resistances obtained using COMSOL (these numbers and how they are computed are explained in Appendix C). From the table, it can be seen that both conductive and convective resistances are decreased for increasing Grashof number. The latter effect is expected due to the increased flow velocity, whereas the former is due to the more compact geometries obtained for higher Grashof numbers. Their combined effect results in increased Biot numbers (ratio between convection and conduction) and also increased effective Nusselt number (average convection coefficient) with increased Grashof number. All these tendencies are to be expected and the well-known fact that increasing Biot number results in shorter and thicker heat fins can also be observed in the optimised topologies. However, the obtained topologies indicate more than that. If the above effect was the only driver for the optimisation, a simple scaled version of the $Gr = 10^3$ design (figure 2a) with shorter and thicker, but mainly circular cross-section fins, would have been obtained for higher Grashof numbers. However, for $Gr = 10^6$ (figure 2d) one clearly observes more vertically oriented walls than circular fin geometries, indicating that the effect of accelerating the fluid at vertical walls plays a major role for higher Grashof numbers. This effect is further illustrated in figure 7, where surface temperature, flux and local Nusselt number are plotted for the designs obtained for $Gr = 10^3$ and $Gr = 10^6$, both evaluated at $Gr = 10^6$. Clearly, the design obtained for $Gr = 10^6$ has lower temperature of the heat source and higher fluxes as expected. On the other hand, the design obtained for $Gr = 10^3$ is seen to have very cold tips, indicating that its elongated fins are inefficient for the higher Grashof number. Also, the local convection coefficients described by Nusselt numbers is seen to be rather constant around and along the fins, whereas the similar values for the $Gr = 10^6$ design are much more non-uniformly distributed, indicating that the fluid flow effects are exploited by the optimised topology to enhance overall heat transfer.

Finally, it should be noted that the obtained temperature distribution is far from being constant, which is not unexpected. Considering simple forced convection heat fins, the optimal temperature profile is linearly decaying with the distance from the heat source and reaches zero at the tip. For natural convection heat fins, a zero temperature difference at the tip is unwanted since this will not accelerate the fluid. On the other hand, a constant temperature is not optimal either, since this would imply zero conductive heat flux in the solid parts. Hence, the optimal topology is an intricate compromise between these conflicting goals and obviously depends strongly on Biot number. The authors conject that topology optimisation is an ideal tool to investigate this interplay in deeper detail. This study will be carried out in future work.

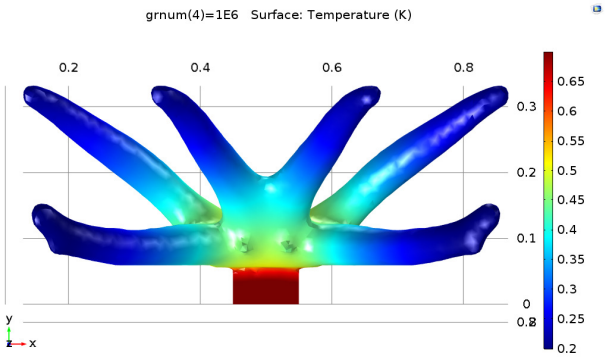

(a) Temperature - $Gr = 10^3$ design

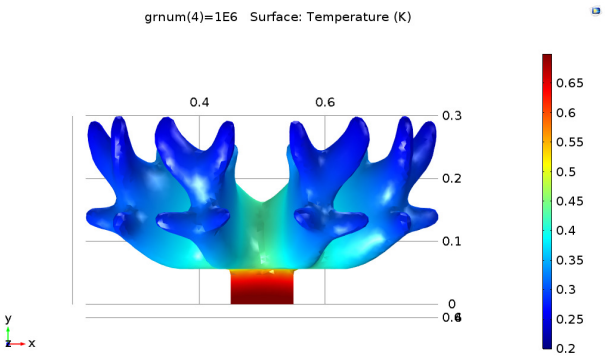

(b) Temperature - $Gr = 10^6$ design

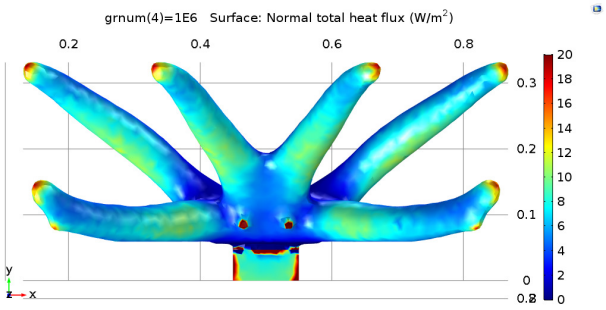

(c) Normal flux - $Gr = 10^3$ design

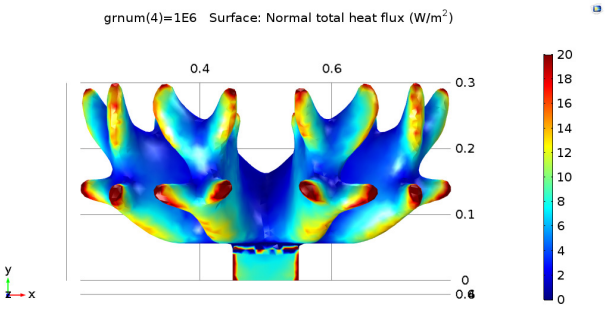

(d) Normal flux - $Gr = 10^6$ design

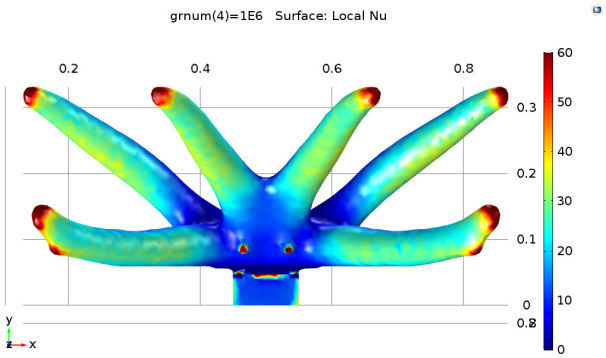

(e) Local Nu_L - $Gr = 10^3$ design

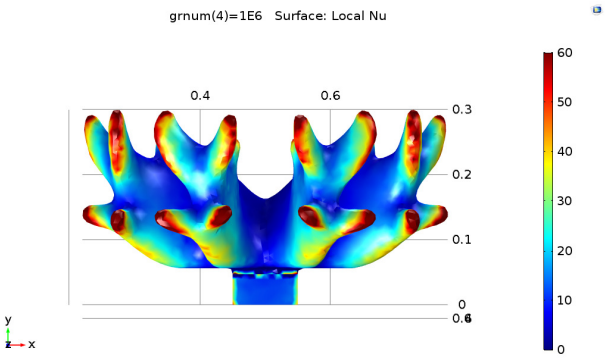

(f) Local Nu_L - $Gr = 10^6$ design

Figure 7: Surface temperature, normal flux and local Nu_L at $Gr = 10^6$ for the designs optimised for $Gr = 10^3$ and $Gr = 10^6$. Units should be disregarded since the simulations have been performed using the same dimensionless parameters as presented in the article.

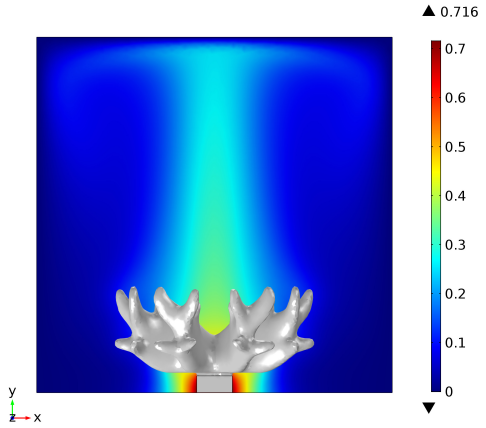

(a) Temperature distribution

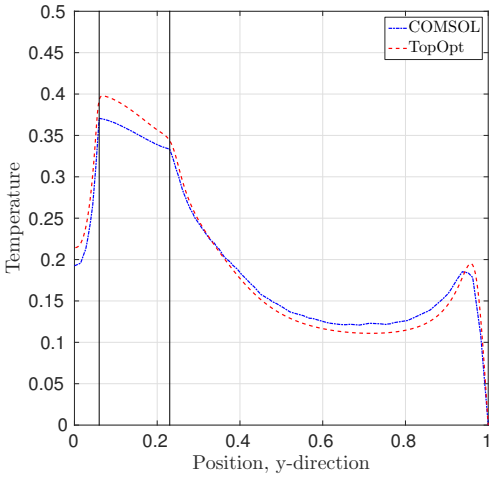

(b) Temperature along line

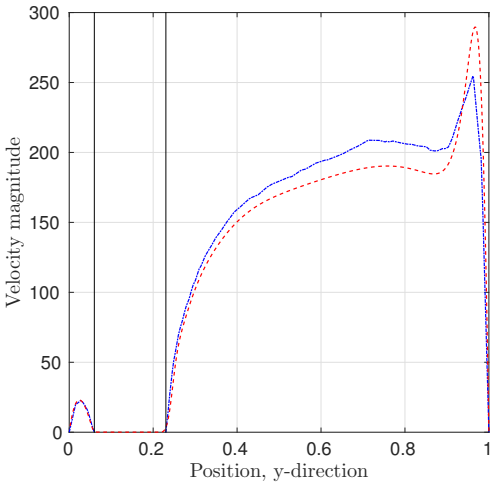

(c) Velocity magnitude along line

Figure 5: Temperature distribution for the verification analysis for $Gr = 10^6$, as well as temperature and velocity fields as a function of y-coordinate at $(x, z) = (0.57, 0.65)$.

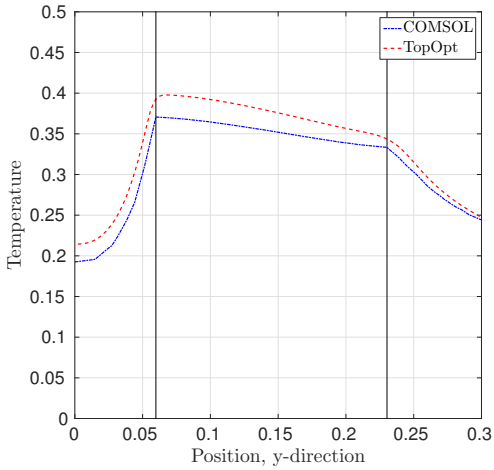

(a) Temperature

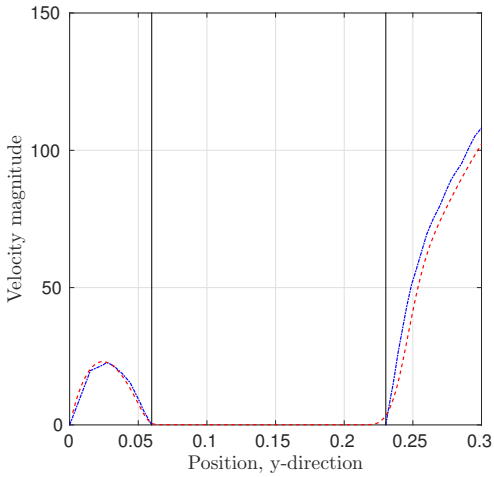

(b) Velocity magnitude

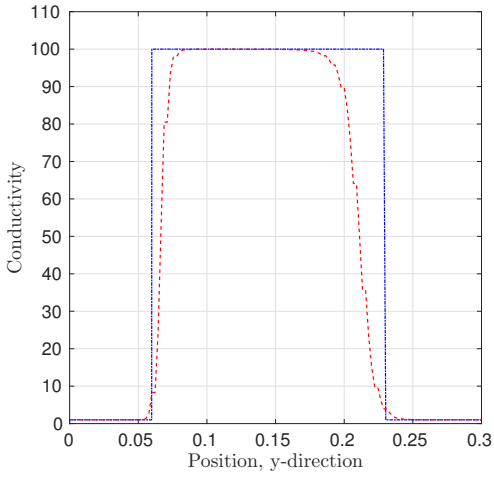

(c) Conductivity

Figure 6: Close up of temperature, velocity and conductivity fields as a function of y-coordinate at $(x, z) = (0.57, 0.65)$.

6.5. High resolution design

The topology optimisation problem is now investigated with a computational mesh of $320 \times 640 \times 320$ elements yielding a total of $65,536,000$ elements and $330,246,405$ degrees of freedom for the quarter domain. The design domain now consists of $27,648,000$ elements and the filter radius is set to 2.5 times the element size, i.e. in absolute measures half the size of before. The optimisation is run for 1000 design iterations and the computational time was 107 and 108 hours, respectively, for $Gr = 10^3$ and $Gr = 10^6$, using 2560 cores. This yields an average of 6.4 and 6.5 minutes per design iteration, respectively.

Figure 8 shows the optimised design for $Gr = 10^6$ with the fine mesh resolution and small length scale at various steps of the continuation strategy. The complexity of the design can be seen to be significantly higher than for the design with a larger length scale, figure 2d. The subfigures are the final iterations of the 1st, 2nd, 3rd and 5th (final) continuation steps. It can be seen that the complexity of the design decreases during the optimisation process once the overall topology has been settled (iteration 400 and onwards). This is due to the harder and harder penalisation of intermediate design field values, with respect to conductivity, which are present at the interface between solid and fluid. Therefore, smaller features are progressively removed as the surface area is more heavily penalised. The reason for going to such high penalisation of the conductivity is to ensure the approximate collocation of the fluid and thermal boundaries, as shown in section 6.4. However, if one starts directly with these physically-relevant parameters, particularly poor local minima have been observed.

Figure 9 shows the final optimised designs for $Gr = 10^3$ and $Gr = 10^6$ with the fine mesh resolution and small length scale. The complexities of both designs can be seen to be significantly higher than the previous, figures 2a and 2d, due to the smaller length scale. The obtained topologies confirm the results from the coarse mesh studies in section 6.3. For low Grashof number the topology consists of simple circular fins (with occasional fingers), whereas the topology obtained for the higher Grashof number constitutes a more complex geometry reflecting the compromise between compactness, surface area and vertical walls for improved flow acceleration.

6.6. Change in boundary conditions

An additional problem is considered, where the boundary conditions for the side walls are changed to insulated. These boundary conditions were investigated in-depth by Coffin and Maute [38] in two dimensions, and briefly in three dimensions. Here, a three-dimensional equivalent of the problem is investigated using a cubic domain. The full domain is analysed, as it was observed in [38] that an asymmetric design is beneficial for these boundary conditions. In order to trigger asymmetric details, the initial design field is seeded with an angular dependency in the xz-plane with relation to the x-axis.

The computational mesh is $160 \times 160 \times 160$ elements yielding a total of $4,096,000$ elements and $20,866,405$ degrees of freedom for the full domain. The design domain consists of $1,728,000$ elements and the filter radius is set to 2.5 times the element size. The optimisation is run for 500 design iterations and the computational time was 10 hours 37 minutes and 10 hours 53 minutes, respectively, for $Gr = 10^3$ and $Gr = 10^4$, using 640 cores. This yields an average of approximately 1.3 minutes per design iteration.

	Gr	
Symmetry	10^3	10^4
Enforced	22.64	14.27
Not enforced	22.25	13.17

Table 9: Objective function values for the designs in cavity with insulated sides.

Figure 10 shows the final optimised designs for $Gr = 10^3$ and $Gr = 10^4$. It is interesting to see that the asymmetry of the optimised designs appears to depend on the Grashof number. This was also observed in two dimensions by Coffin and Maute [38]. In order to compare the asymmetric designs to equivalent symmetric designs, the problem is also analysed by enforcing quarter symmetry. Figure 11 shows the final optimised quarter symmetric designs for $Gr = 10^3$ and $Gr = 10^4$. By comparing figures 10 and 11, it can be seen that for $Gr = 10^3$, the design remains close to symmetric, but as convection-dominance is increased, $Gr = 10^4$, the design becomes asymmetric to a large degree.

Table 9 compares the objective function values for enforced quarter symmetry and the free design. It can be seen that the asymmetric designs perform better for both Grashof numbers, but that the difference is most significant for $Gr = 10^4$.

The designs observed for $Gr = 10^3$ is similar in appearance as the three-dimensional design in [38] for very similar parameter values. The design clearly shows that the goal is now to conduct the heat to the very top of the domain for the diffusion-dominant problem, but this quickly changes for increasing convection-dominance where the possibility of an asymmetric flow is taken advantage of.

The problem has only been investigated for $Gr = 10^3$ and $Gr = 10^4$, as convergence issues (non-linear state solver) were encountered for higher Grashof numbers when treating the full domain. However, when enforcing quarter symmetry (in both the design and state solutions), higher Grashof numbers ($Gr = 10^5$ and $Gr = 10^6$) could be optimised without problems. This is likely due to the fact that the flow becomes unstable for higher Grashof numbers when allowing for asymmetric designs. In order to optimise for these conditions, one has to use a transient solver and optimisation routine, e.g. [26, 38].

It can be seen that for this particular choice of boundary conditions, an asymmetric design performs better than a quarter symmetric design. This is not the case when the side walls are kept at the same cold temperature as the top, figure 2. The adiabatic walls allow for the flow parallel to the wall to move in both the upward and downward directions. However, when they are cold, as for the initial problem, the flow is essentially forced to descend at the side walls. The adiabatic walls allows for the fluid to ascend on some sides and the flow to collect into a single main convection roll, in turn minimising viscous losses. With cold side walls, the flow is pretty much hard set

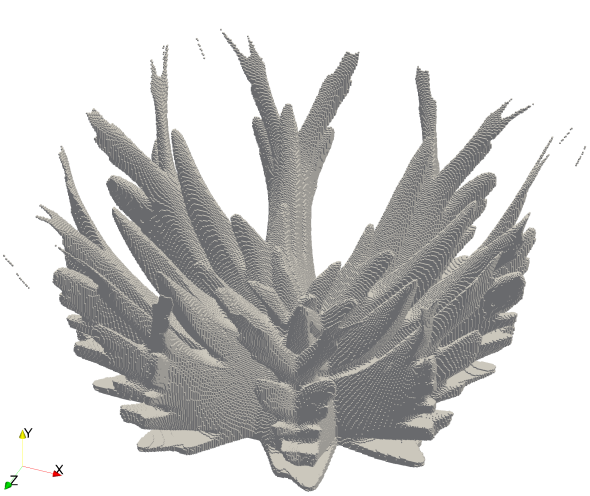

(a) Iteration 200

(b) Iteration 400

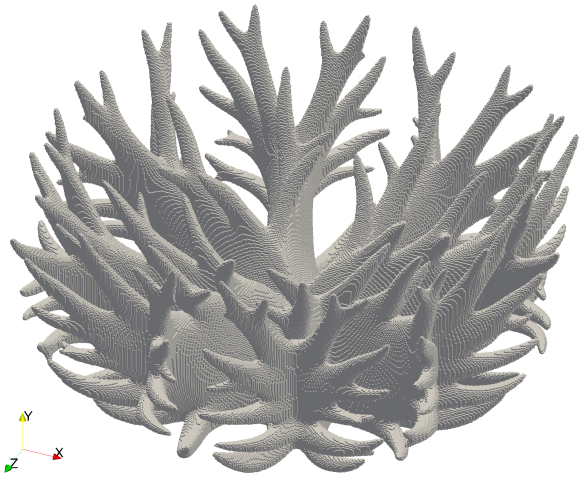

(c) Iteration 600

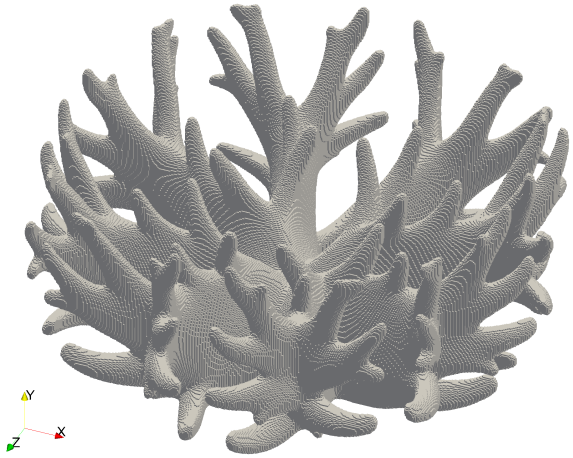

(d) Iteration 1000

Figure 8: Optimised designs for $Gr = 10^6$ at a mesh resolution of $320 \times 640 \times 320$. Please note that the freely hanging material in (a) is due to only elements below the threshold, $\gamma = 0.05$, are shown - the design is connected by intermediate design field values.

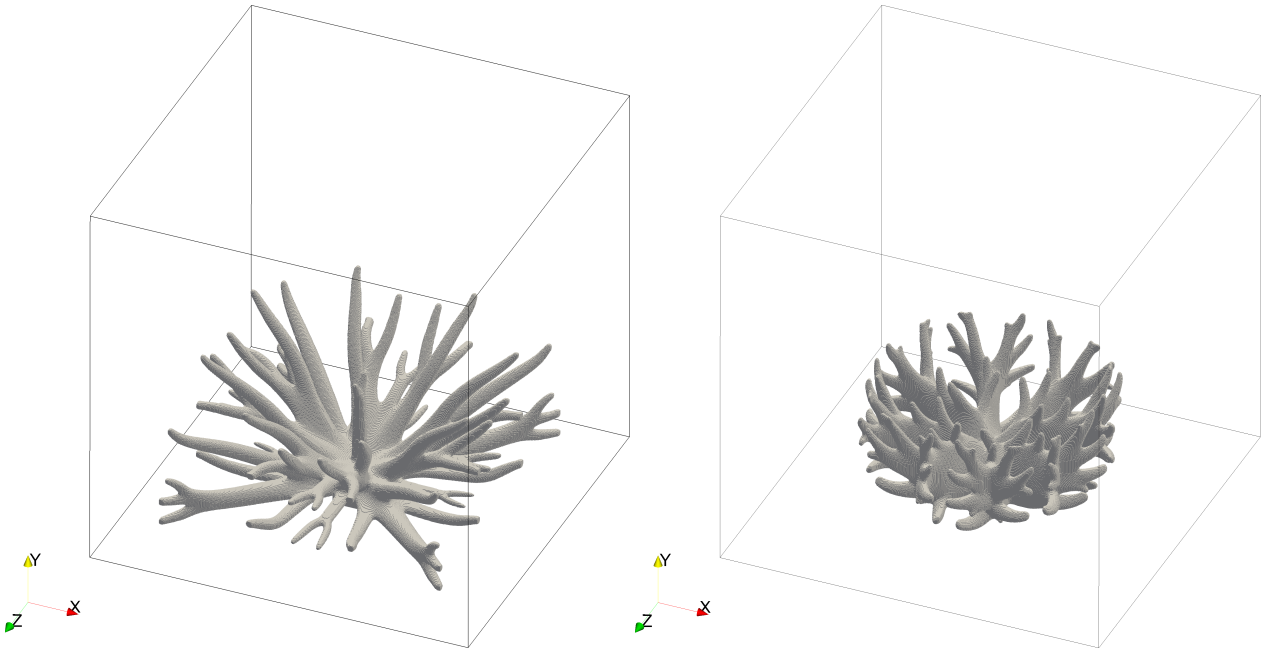

(a) $Gr = 10^3$ (b) $Gr = 10^6$

Figure 9: Optimised designs for $Gr = 10^3$ and $Gr = 10^6$ at a mesh resolution of $320 \times 640 \times 320$. The outline of the outer walls are shown in black.

to four main convection rolls with the solid member in the middle. It is interesting to note, that contrary to observations in two dimensions [38], the maximum velocity is significantly lower (37.5) for the asymmetric design than for the quarter symmetric design (50.7). Based on the observations from the steady state solver regarding stability, it is postulated that the extra constrained conditions, may also provide a stabilising effect and move the critical Grashof number upwards, allowing for steady-state solutions at higher Grashof numbers.

7. Discussion and conclusion

In this article, topology optimisation has been applied to the design of three-dimensional heat sinks using a fully coupled non-linear thermofluidic model. In contrast to previous works within topology optimisation, that considered simplified convection models, the presented methodology is able to recover interesting physical effects and insights, and avoids problems with the formation of non-physical internal cavities, length-scale effects and artificial convection assumptions. The implementation of the code in a PETSc framework suitable for large scale parallel computations allows for running examples with more than 300 million degrees of freedom and almost 30 million design variables on regular grids.

The obtained topology optimisation results are verified with the commercial finite element code COMSOL and show consistent results. Field distributions from the hexahedral mesh used in the topology optimisation are in good agreement with results obtained with a smoothed geometry and body-fitted mesh in COMSOL. Furthermore, optimisation results are consistent, i.e. topologies optimised for a certain Grashof number are also the best for that Grashof number when modelled in Comsol.

The examples considered to verify the presented framework are primarily academic in nature. Nevertheless, some interesting insight is obtained, showing that optimised structures go from exhibiting simple branches that conduct heat towards the cold outer boundaries for diffusion-dominated problems, towards complex and compact multi-branched structures that maximise the convection heat transfer for higher Grashof numbers. The observation that lower rates of natural convection produce fewer longer fins, while higher rates of natural convection produce a greater number of short fins/branches are consistent with prior optimisation literature. However, the optimisation also suggests structures that are good at accelerating fluid, in turn ensuring enhanced overall heat transfer, and it should be stressed that here the designs appear spontaneously, without any predefined knowledge or restriction on the design.

Current and future work includes applications to real life problems (see preliminary work in [39]), irregular meshes, multiple orientations, as well as the extension to transient and turbulent problems. Investigations into enhanced accuracy of the boundary layer for highly convection-dominated problems is also of primary interest.

8. Acknowledgements

This work was funded by Villum Fonden through the Next-Top project, as well as by Innovation Fund Denmark through the HyperCool project. The first author was also partially funded by the EU FP7-MC-IAPP programme LaScISO.

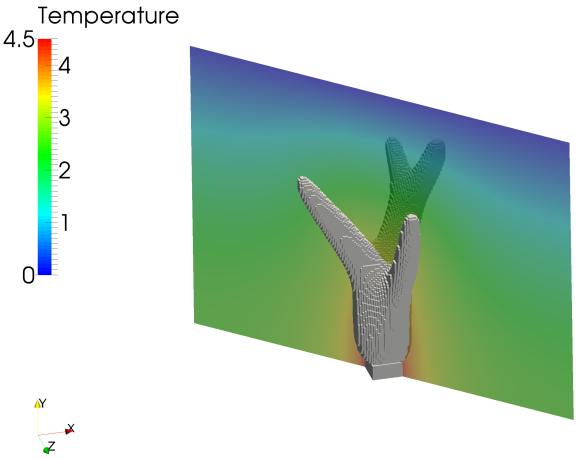

(a) Temperature - $Gr = 10^3$

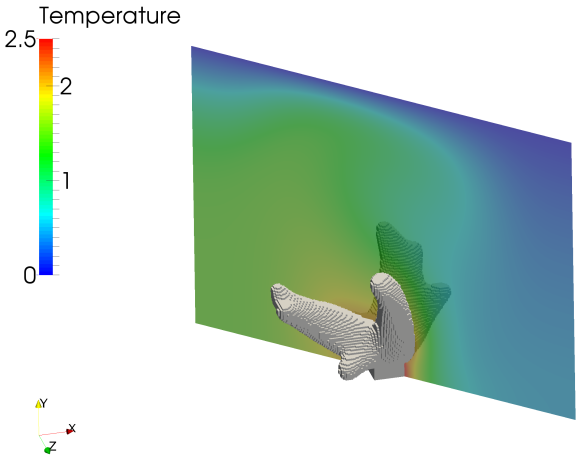

(b) Temperature - $Gr = 10^4$

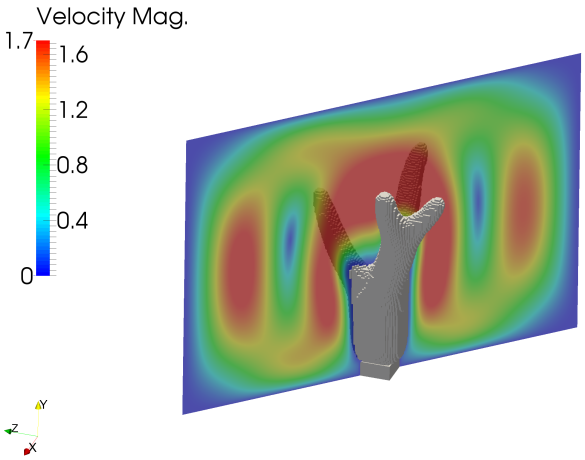

(c) Velocity - $Gr = 10^3$

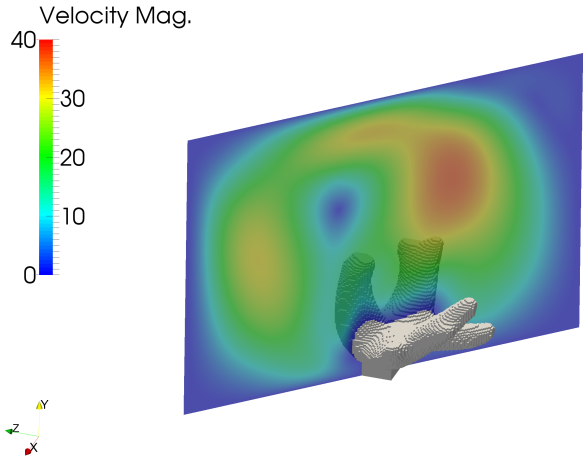

(d) Velocity - $Gr = 10^4$

Figure 10: Optimised designs for $Gr = 10^3$ and $Gr = 10^4$ for cavity with insulated sides.

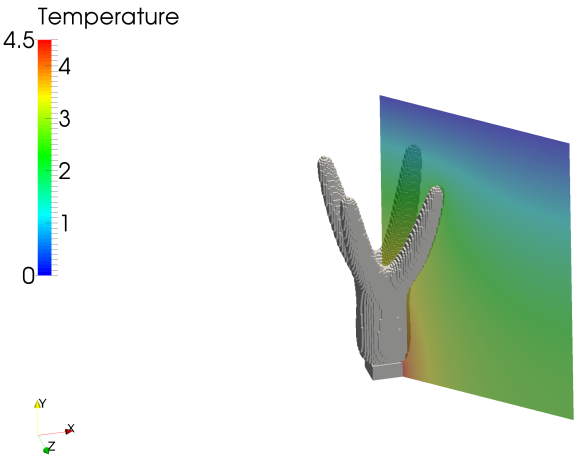

(a) $Gr = 10^3$

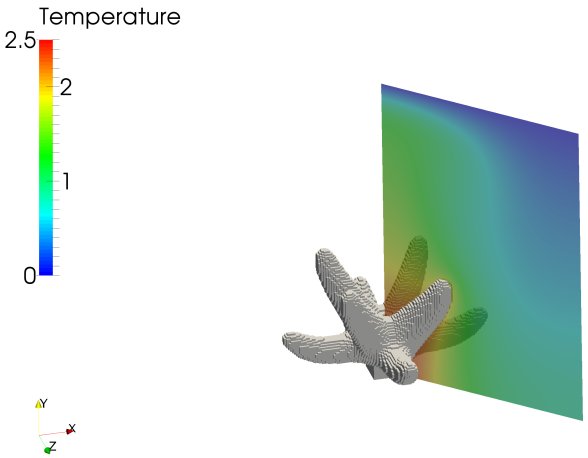

(b) $Gr = 10^4$

Figure 11: Optimised quarter symmetric designs for $Gr = 10^3$ and $Gr = 10^4$ for cavity with insulated sides.

The anonymous reviewers are thanked for their insightful suggestions for improving the article.

Appendix A. Stabilisation parameters

The stabilised weak form of the governing equations are given in [18]. The governing equations are stabilised using the pressure-stabilising Petrov-Galerkin (PSPG) [60, 61] and streamline-upwind Petrov-Galerkin (SUPG) methods [62], for more information please see [18].

The stabilisation parameters for SUPG and PSPG are defined as one and the same using the following approximate min-function:

$$\tau_{SU} = \tau_{PS} = \tau = \left(\frac{1}{{\tau_1}^2} + \frac{1}{{\tau_2}^2} + \frac{1}{{\tau_3}^2} \right)^{-\frac{1}{2}} \tag{A.1}$$

The limit factors are given by:

$$\tau_1 = \frac{4h_e}{\|\mathbf{u}_e\|_2} \tag{A.2a}$$

$$\tau_2 = \frac{{h_e}^2}{4Pr} \tag{A.2b}$$

$$\tau_3 = \frac{1}{\alpha_e} \tag{A.2c}$$

where h_e is a characteristic element size (for cubes the element edge length) and $\mathbf{u}_e$ is the element vector of velocity degrees of freedom. The first limit factor, τ_1, has been simplified based on evaluation at element centroids under the assumption of a single Gauss-point, yielding a constant stabilisation factor within each element.

In order to define a consistent Jacobian matrix, and thus a consistent adjoint problem, the derivatives of the stabilisation factors are needed with respect to the velocity field. This can be found to be:

$$\frac{\partial \tau}{\partial \mathbf{u}_e} = -\tau \left(1 + \left(\frac{\tau_1}{\tau_2} \right)^2 + \left(\frac{\tau_1}{\tau_3} \right)^2 \right)^{-1} \left({\mathbf{u}_e}^{\mathrm{T}} \mathbf{u}_e \right)^{-1} {\mathbf{u}_e}^{\mathrm{T}} \tag{A.3}$$

Furthermore, to define consistent design sensitivities, the derivatives of the stabilisation factors with respect to the design field is needed. This can be found to be:

$$\frac{\partial \tau}{\partial \gamma_e} = -\frac{\tau}{\tau_3} \left(\left(\frac{\tau_3}{\tau_1} \right)^2 + \left(\frac{\tau_3}{\tau_2} \right)^2 + 1 \right)^{-1} \frac{\partial \alpha_e}{\partial \gamma_e} \tag{A.4}$$

Including the derivatives in the definition of consistent adjoint sensitivities has been observed to provide a one to two order of magnitude improvement in accuracy of sensitivities with respect to a finite difference approximation. Significant differences have not been observed in optimisation behaviour or in final designs. However, this cannot be guaranteed in general and it is therefore best to ensure consistency, as also highlighted by the similar issue of frozen turbulence [63].

Similar definitions and derivations are carried out for the thermal SUPG stabilisation.

Computational Gr	Mesh	Figure	Actual Gr
10^3	$160 \times 320 \times 160$	2a	1.69×10^3
10^4	$160 \times 320 \times 160$	2b	1.55×10^4
10^5	$160 \times 320 \times 160$	2c	1.16×10^5
10^6	$160 \times 320 \times 160$	2d	8.60×10^5
10^3	$320 \times 640 \times 320$	9a	1.42×10^3
10^6	$320 \times 640 \times 320$	9b	7.16×10^5
10^3	$160 \times 160 \times 160$	10a	4.49×10^3
10^4	$160 \times 160 \times 160$	10b	2.68×10^4
10^3	$80 \times 160 \times 80$	11a	4.57×10^3
10^4	$80 \times 160 \times 80$	11b	2.89×10^4

Table B.10: Computational and actual Gr-numbers for the designs presented in this article.

Appendix B. Computational versus actual Grashof number

The Grashof numbers used above are all based on an *a priori* defined reference temperature difference. However, the actual temperature difference observed between the heat source and the walls are not known *a priori* due to the fact that the problem only has a single known temperature (Dirichlet boundary condition) and a volumetric heat source. This is why the maximum temperature observed for the designs, see figure 2, is not equal to 1. Therefore, after the optimisation, one can define an *a posteriori* Grashof number based on the actual computed temperature difference. The *a priori* version can be termed the computational Grashof number, the one that goes into the dimensionless governing equations; and the *a posteriori* version can be called the actual, or optimised, Grashof number for the given optimised design. The actual Grashof number can be useful for experimental studies, as well as for future comparisons.

The temperature scale used in the calculation of the Grashof number is arbitrary for computational purposes, as it merely scales the non-dimensional temperature field. Thus, if a smaller temperature scale is used, the non-dimensional temperature increases proportionally; and if a larger temperature scale is used, the non-dimensional temperature decreases proportionally. Assuming full precision arithmetic, the final designs, obtained for two arbitrarily chosen temperature scales, should be the same. Working with finite precision arithmetic, this of course cannot be guaranteed.

The actual Grashof numbers for the designs shown in this article are listed in Table B.10. The values for the finer meshes are lower due to the lower thermal compliance, equivalent to the temperature of the heat source, allowed by the smaller design length scale.

Appendix C. Calculation of thermal resistances and Nusselt number

Asterisks denote dimensional quantities related to the unasterisked non-dimensional equivalents. It is assumed, without loss of generality, that the free flow temperature and the reference temperature, T_0, are the same.

Appendix C.1. Thermal resistance analysis

It is assumed that the heat loss from the sides of the heat source is neglectable, to simplify the analysis. Using the verification calculations, this has been confirmed. All power from the heat source is thus assumed to pass through the heat sink surface. For an introduction to thermal resistance analysis, please see e.g. [64].

The conductive resistance is defined as:

$$R^*_{cond} = \frac{T^*_b - T^*_s}{Q^*} \tag{C.1}$$

where T^*_b is the temperature of the base (heat source) and T^*_s is the temperature of the heat sink surface. Furthermore, Q^* is the total power of the heat source:

$$Q^* = \int_\omega q^* dV^* = q^* \omega^* \tag{C.2}$$

where ω^* is the volume of the heat source.

Equation C.1 is non-dimensionalised using the same quantities as the governing equations [18], yielding:

$$R^*_{cond} = \frac{1}{k_f L} R_{cond} \tag{C.3}$$

where the non-dimensional conductive resistance is defined as:

$$R_{cond} = \frac{T_b - T_s}{s_0 \omega} \tag{C.4}$$

An equivalent non-dimensionalisation is performed for the convective resistance:

$$R^*_{conv} = \frac{T^*_s - T_0}{Q^*} = \frac{1}{k_f L} R_{conv} \tag{C.5}$$

where the non-dimensional convective resistance is defined as:

$$R_{conv} = \frac{T_s}{s_0 \omega} \tag{C.6}$$

According to e.g. [64], the Biot number can be defined as the ratio of the conductive resistance to convective resistance. This gives:

$$Bi_{res} = \frac{R^*_{cond}}{R^*_{conv}} = \frac{R_{cond}}{R_{conv}} = \frac{T_b - T_s}{T_s} \tag{C.7}$$

Looking at this expression clearly shows that Bi_{res} represents a measure of the isothermality of the heat sink geometry.

In order to use the above expressions for the complex three-dimensional heat sink geometries presented, T_b is defined to be the volume-averaged temperature of the base (heat source):

$$T_b = \frac{1}{\omega} \int_\omega T dV \tag{C.8}$$

and T_s to be the surface-averaged temperature of the surface:

$$T_s = \frac{1}{A_{hs}} \int_{\Gamma_{hs}} T dS \tag{C.9}$$

where Γ_{hs} is the heat sink surface and A_{hs} the area thereof.

Appendix C.2. Nusselt number

Newton's law of cooling gives the relation between the local normal flux, $q^{''^*}_n$, and the convection heat transfer coefficient, h:

$$q^{''^*}_n = h(T^* - T_0) \tag{C.10}$$

From this, one can isolate the convection coefficient and define an effective heat transfer coefficient, $\overline{h}$, as the surface-averaged quantity:

$$\overline{h} = \frac{1}{A^*_{hs}} \int_{\Gamma_{hs}} \frac{q^{''^*}_n}{T^* - T_0} dS^* \tag{C.11}$$

Equation C.11 is non-dimensionalised yielding:

$$\overline{h} = \frac{k_f}{L} \cdot \frac{1}{A_{hs}} \int_{\Gamma_{hs}} \frac{q^{''}_n}{T} dS \tag{C.12}$$

From this, the effective Nusselt number, based on the reference length of the problem, can be defined as:

$$\overline{Nu}_L = \frac{\overline{h} L}{k_f} = \frac{1}{A_{hs}} \int_{\Gamma_{hs}} \frac{q^{''}_n}{T} dS \tag{C.13}$$

By looking at the physical arguments and the origin of the expression, it can be seen that the effective Nusselt number represents a non-dimensional effective heat transfer coefficient.

A local Nusselt number equivalent to the local convection coefficient, h, is simply defined as:

$$Nu_L = \frac{hL}{k_f} = \frac{q^{''}_n}{T} \tag{C.14}$$

References

[1] A. T. Morrison, Optimization of heat sink fin geometries for heat sinks in natural convection, in: InterSociety Conference on Thermal Phenomena in Electronic Systems, I-THERM III, 1992, pp. 145–148. doi:10.1109/ITHERM.1992.187753.

[2] G. Ledezma, A. Bejan, Optimal geometric arrangement of staggered vertical plates in natural convection, Journal of Heat Transfer 119 (4) (1997) 700–708. doi:10.1115/1.2824174.

[3] M. Iyengar, A. B. Cohen, Least-material optimization of vertical pin-fin, plate-fin, and triangular-fin heat sinks in natural convective heat transfer, in: Thermal and Thermomechanical Phenomena in Electronic Systems, 1998. ITHERM'98. The Sixth Intersociety Conference on, IEEE, 1998, pp. 295–302.

[4] R. Bahadur, A. Bar-Cohen, Thermal design and optimization of natural convection polymer pin fin heat sinks, IEEE Transactions on Components and Packaging Technologies 28 (2) (2005) 238–246. doi:10.1109/TCAPT.2005.848498.

[5] D. Jang, S.-H. Yu, K.-S. Lee, Multidisciplinary optimization of a pin-fin radial heat sink for led lighting applications, International Journal of Heat and Mass Transfer 55 (4) (2012) 515–521. doi:10.1016/j.ijheatmasstransfer.2011.11.016.

[6] A. Bejan, Constructal-theory network of conducting paths for cooling a heat generating volume, International Journal of Heat and Mass Transfer 40 (4) (1997) 799–816. doi:10.1016/0017-9310(96)00175-5.

[7] M. P. Bendsøe, O. Sigmund, Topology Optimization: Theory, Methods and Applications, Springer, 2003, ISBN: 3-540-42992-1.

[8] O. Sigmund, K. Maute, Topology optimization approaches, Structural and Multidisciplinary Optimization 48 (6) (2013) 1031–1055. doi:10.1007/s00158-013-0978-6.

[9] J. D. Deaton, R. V. Grandhi, A survey of structural and multidisciplinary continuum topology optimization: post 2000, Structural and Multidisciplinary Optimization 49 (1) (2013) 1–38. doi:10.1007/s00158-013-0956-z.

[10] L. Yin, G. Ananthasuresh, A novel topology design scheme for the multi-physics problems of electro-thermally actuated compliant micromechanisms, Sensors and Actuators 97-98 (2002) 599–609. doi:10.1016/S0924-4247(01)00853-6.

[11] T. Bruns, Topology optimization of convection-dominated, steady-state heat transfer problems, International Journal of Heat and Mass Transfer 50 (15-16) (2007) 2859–2873. doi:10.1016/j.ijheatmasstransfer.2007.01.039.

[12] A. Iga, S. Nishiwaki, K. Izui, M. Yoshimura, Topology optimization for thermal conductors considering design-dependent effects, including heat conduction and convection, International Journal of Heat and Mass Transfer 52 (11-12) (2009) 2721–2732. doi:10.1016/j.ijheatmasstransfer.2008.12.013.

[13] J. Alexandersen, Topology optimisation for convection problems, B.Eng. thesis, Technical University of Denmark (2011).
URL http://orbit.dtu.dk/en/

[14] E. Dede, S. N. Joshi, F. Zhou, Topology optimization, additive layer manufacturing, and experimental testing of an air-cooled heat sink, ASME Journal of Mechanical Design 137 (11). doi:10.1115/1.4030989.

[15] M. Zhou, J. Alexandersen, O. Sigmund, C. B. W. Pedersen., Industrial application of topology optimization for combined conductive and convective heat transfer problems, Structural and Multidisciplinary Optimization online first (2016) 1–16. doi:10.1007/s00158-016-1433-2.

[16] P. Coffin, K. Maute, Level set topology optimization of cooling and heating devices using a simplified convection model, Structural and Multidisciplinary Optimization (2015) 1–19doi:10.1007/s00158-015-1343-8.

[17] J. Alexandersen, Topology optimisation for axisymmetric convection problems, Tech. rep., Technical University of Denmark (2011).
URL http://orbit.dtu.dk/en/

[18] J. Alexandersen, N. Aage, C. S. Andreasen, O. Sigmund, Topology optimisation of natural convection problems, International Journal for Numerical Methods in Fluids 76 (10) (2014) 699–721. doi:10.1002/fld.3954.

[19] T. Borrvall, J. Petersson, Topology optimization of fluids in Stokes flow, International Journal for Numerical Methods in Fluids 41 (1) (2003) 77–107. doi:10.1002/fld.426.

[20] A. Gersborg-Hansen, O. Sigmund, R. Haber, Topology optimization of channel flow problems, Structural Multidisciplinary Optimization 30 (3) (2005) 181–192. doi:10.1007/s00158-004-0508-7.

[21] C. S. Andreasen, A. R. Gersborg, O. Sigmund, Topology optimization of microfluidic mixers, International Journal for Numerical Methods in Fluids 61 (5) (2009) 498–513. doi:10.1002/fld.1964.

[22] D. Makhija, K. Maute, Level set topology optimization of scalar transport problems, Structural and Multidisciplinary Optimization 51 (2) (2015) 267–285. doi:10.1007/s00158-014-1142-7.

[23] F. Okkels, H. Bruus, Scaling behavior of optimally structured catalytic microfluidic reactors, Phys. Rev. E 75 (1) (2007) 016301. doi:10.1103/PhysRevE.75.016301.

[24] S. Kreissl, G. Pingen, K. Maute, Topology optimization for unsteady flow, International Journal for Numerical Methods in Engineering 87 (13) (2011) 1229–1253. doi:10.1002/nme.3151.

[25] Y. Deng, Z. Liu, P. Zhang, Y. Liu, Y. Wu, Topology optimization of unsteady incompressible Navier-Stokes flows, Journal of Computational Physics 230 (17) (2011) 6688–6708. doi:10.1016/j.jcp.2011.05.004.

[26] S. Nørgaard, O. Sigmund, B. Lazarov, Topology optimization of unsteady flow problems using the lattice boltzmann method, Journal of Computational Physics 307 (2016) 291 – 307. doi:10.1016/j.jcp.2015.12.023.

[27] G. H. Yoon, Topology optimization for stationary fluid-structure interaction problems using a new monolithic formulation, International Journal for Numerical Methods in Engineering 82 (5) (2010) 591–616. doi:10.1002/nme.2777.

[28] N. Jenkins, K. Maute, Level set topology optimization of stationary fluid-structure interaction problems, Structural and Multidisciplinary Optimization 52 (1) (2015) 179–195. doi:10.1007/s00158-015-1229-9.

[29] E. A. Kontoleontos, E. M. Papoutsis-Kiachagias, A. S. Zymaris, D. I. Papadimitriou, K. C. Giannakoglou, Adjoint-based constrained topology optimization for viscous flows, including heat transfer, Engineering Optimization 45 (8) (2013) 941–961. doi:10.1080/0305215X.2012.717074.

[30] E. Dede, Multiphysics topology optimization of heat transfer and fluid flow systems, in: Proceedings of the COMSOL Conference 2009 Boston, 2009.

[31] G. H. Yoon, Topological design of heat dissipating structure with forced convective heat transfer, Journal of Mechanical Science and Technology 24 (6) (2010) 1225–1233. doi:10.1007/s12206-010-0328-1.

[32] K. Lee, Topology optimization of convective cooling system designs, Ph.D. thesis, University of Michigan (2012).
URL http://deepblue.lib.umich.edu

[33] A. A. Koga, E. C. C. Lopes, H. F. V. Nova, C. R. de Lima, E. C. N. Silva, Development of heat sink device by using topology optimization, International Journal of Heat and Mass Transfer 64 (2013) 759–772. doi:10.1016/j.ijheatmasstransfer.2013.05.007.

[34] G. Marck, M. Nemer, J.-L. Harion, Topology optimization of heat and mass transfer problems: Laminar flow, Numerical Heat Transfer, Part B: Fundamentals 63 (6) (2013) 508–539. doi:10.1080/10407790.2013.772001.

[35] J. H. K. Haertel, K. Engelbrecht, B. S. Lazarov, O. Sigmund, Topology optimization of thermal heat sinks, in: Proceedings of COMSOL conference 2015, 2015.

[36] K. Yaji, T. Yamada, M. Yoshino, T. Matsumoto, K. Izui, S. Nishiwaki, Topology optimization in thermal-fluid flow using the lattice boltzmann method, Journal of Computational Physics 307 (2016) 355 – 377. doi:10.1016/j.jcp.2015.12.008.

[37] L. Laniewski-Wollk, J. Rokicki, Adjoint lattice boltzmann for topology optimization on multi-gpu architecture, Computers & Mathematics with Applications 71 (3) (2016) 833 – 848. doi:http://dx.doi.org/10.1016/j.camwa.2015.12.043.

[38] P. Coffin, K. Maute, A level-set method for steady-state and transient natural convection problems, Structural and Multidisciplinary Optimization (2015) 1–21doi:10.1007/s00158-015-1377-y.

[39] J. Alexandersen, O. Sigmund, N. Aage, Topology optimisation of passive coolers for light-emitting diode lamps, in: 11th World Congress on Structural and Multidisciplinary Optimization, 2015. doi:10.13140/RG.2.1.3906.5446.
URL www.aeromech.usyd.edu.au/WCSMO2015/papers/1264_paper.pdf

[40] E. Andreassen, A. Clausen, M. Schevenels, B. S. Lazarov, O. Sigmund, Efficient topology optimization in MATLAB using 88 lines of code, Structural and Multidisciplinary Optimization 43 (2011) 1–16. doi:10.1007/s00158-010-0594-7.

[41] O. Amir, N. Aage, B. S. Lazarov, On multigrid-CG for efficient topology optimization, Structural and Multidisciplinary Optimization (2013) 1–15doi:10.1007/s00158-013-1015-5.

[42] J. Alexandersen, B. S. Lazarov, Topology optimisation of manufacturable microstructural details without length scale separation using a spectral coarse basis preconditioner, Computer Methods in Applied Mechanics and Engineering 290 (2015) 156–182. doi:10.1016/j.cma.2015.02.028.

[43] T. H. Nguyen, G. H. Paulino, J. Song, C. H. Le, Improving multiresolution topology optimization via multiple discretizations, International Journal for Numerical Methods in Engineering 92 (6) (2012) 507–530. doi:10.1002/nme.4344.

[44] T. Borrvall, J. Petersson, Large-scale topology optimization in 3D using parallel computing, Computer Methods in Applied Mechanics and Engineering 190 (2001) 6201–6229. doi:10.1016/S0045-7825(01)00216-X.

[45] A. Evgrafov, C. J. Rupp, K. Maute, M. L. Dunn, Large-scale parallel topology optimization using a dual-primal substructuring solver, Structural and Multidisciplinary Optimization 36 (2008) 329–345. doi:10.1007/s00158-007-0190-7.

[46] N. Aage, B. Lazarov, Parallel framework for topology optimization using the method of moving asymptotes, Structural and Multidisciplinary Optimization 47 (4) (2013) 493–505. doi:10.1007/s00158-012-0869-2.

[47] N. Aage, E. Andreassen, B. S. Lazarov, Topology optimization using PETSc: An easy-to-use, fully parallel, open source topology optimization framework, Structural and Multidisciplinary Optimization 51 (3) (2014) 565–572. doi:10.1007/s00158-014-1157-0.

[48] S. Balay, S. Abhyankar, M. F. Adams, J. Brown, P. Brune, K. Buschelman, V. Eijkhout, W. D. Gropp, D. Kaushik, M. G. Knepley, L. C. McInnes, K. Rupp, B. F. Smith, H. Zhang, PETSc Users Manual, Tech. Rep. ANL-95/11 - Revision 3.5, Argonne National Laboratory (2014).
URL http://www.mcs.anl.gov/petsc

[49] B. S. Lazarov, O. Sigmund, Filters in topology optimization based on Helmholtz-type differential equations, International Journal for Numerical Methods in Engineering 86 (2011) 765–781. doi:10.1002/nme.3072.

[50] K. Svanberg, The method of moving asymptotes - a new method for structural optimization, International Journal for Numerical Methods in Engi-

neering 24 (2) (1987) 359–373. doi:10.1002/nme.1620240207.

[51] M. Stolpe, K. Svanberg, On the trajectories of penalization methods for topology optimization, Structural Multidisciplinary Optimization 21 (2001) 128–139. doi:10.1007/s001580050177.

[52] S. Rojas-Labanda, M. Stolpe, Benchmarking optimization solvers for structural topology optimization, Structural and Multidisciplinary Optimization 52 (3) (2015) 527–547. doi:10.1007/s00158-015-1250-z.

[53] P. S. Vassilevski, Multilevel Block Factorization Preconditioners, Springer, 2007. doi:10.1007/978-0-387-71564-3.

[54] F. Wang, B. S. Lazarov, O. Sigmund, On projection methods, convergence and robust formulations in topology optimization, Structural Multidisciplinary Optimization 43 (6) (2011) 767–784. doi:10.1007/s00158-010-0602-y.

[55] M. Zhou, B. S. Lazarov, F. Wang, O. Sigmund, Minimum length scale in topology optimization by geometric constraints, Computer Methods in Applied Mechanics and Engineering 293 (2015) 266 – 282. doi:10.1016/j.cma.2015.05.003.

[56] B. S. Lazarov, F. Wang, O. Sigmund, Length scale and manufacturability in density-based topology optimization, Archive of Applied Mechanics (2016) 1–30doi:10.1007/s00419-015-1106-4.

[57] A. N. Christiansen, M. Nobel-Jørgensen, N. Aage, O. Sigmund, J. A. Bærentzen, Topology optimization using an explicit interface representation, Structural and Multidisciplinary Optimization 49 (3) (2013) 387–399. doi:10.1007/s00158-013-0983-9.

[58] A. N. Christiansen, J. A. Brentzen, M. Nobel-Jrgensen, N. Aage, O. Sigmund, Combined shape and topology optimization of 3d structures, Computers & Graphics 46 (2015) 25 – 35, shape Modeling International 2014. doi:http://dx.doi.org/10.1016/j.cag.2014.09.021.

[59] D. Makhija, K. Maute, Numerical instabilities in level set topology optimization with the extended finite element method, Structural and Multidisciplinary Optimization 49 (2) (2013) 185–197. doi:10.1007/s00158-013-0982-x.

[60] T. J. Hughes, L. P. France, M. Balestra, A new finite element formulation for computational fluid dynamics V - circumventing the Babuska-Brezzi condition: a stable Petrov-Galerkin formulation of the Stokes problem accomodating equal-order interpolations, Computer Methods in Applied Mechanics and Engineering 59 (1) (1986) 85–99. doi:10.1016/0045-7825(86)90025-3.

[61] T. E. Tezduyar, S. Mittal, S. Ray, R. Shih, Incompressible flow computations with stabilized bilinear and linear equal-order-interpolation velocity-pressure elements, Computer Methods in Applied Mechanics and Engineering 95 (2) (1992) 221–242. doi:10.1016/0045-7825(92)90141-6.

[62] A. N. Brooks, T. J. Hughes, Streamline Upwind/Petrov-Galerkin formulations for convection dominated flows with particular emphasis on the incompressible Navier-Stokes equations, Computer Methods in Applied Mechanics and Engineering 32 (1-3) (1982) 199–259. doi:10.1016/0045-7825(82)90071-8.

[63] A. S. Zymaris, D. I. Papadimitriou, K. C. Giannakoglou, C. Othmer, Continuous adjoint approach to the spalart-allmaras turbulence model for incompressible flows, Computers and Fluids 38 (2009) 1528–1538. doi:doi:10.1016/j.compfluid.2008.12.006.

[64] F. P. Incropera, D. P. DeWitt, T. L. Bergman, A. S. Lavine, Introduction to Heat Transfer, 5th Edition, Wiley, 2007, iSBN: 978-0-471-45727-5.